ACS APPLIED NANO MATERIALS
Cite This: ACS Appl. Nano Mater. 2018, 1, 820−830
Article
www.acsanm.org

# Multifunctional Bismuth Nanoparticles as Theranostic Agent for PA/CT Imaging and NIR Laser-Driven Photothermal Therapy

Chunyu Yang,[†,§] Chongshen Guo,[‡,§] Wei Guo,[‡] Xiaole Zhao,[†] Shaoqin Liu,*[,‡] and Xiaojun Han*[,†]

[†]State Key Laboratory of Urban Water Resource and Environment, School of Chemistry and Chemical Engineering, Harbin Institute of Technology, Harbin 150001, China

[‡]Key Lab of Microsystem and Microstructure Manufacturing (Ministry of Education), Academy of Fundmental and Interdisciplinary Sciences, Harbin Institute of Technology, Harbin 150080, China

Supporting Information

**ABSTRACT:** "One-for-all" multifunctional theranostic agents are highly demanded in biomedical fields. However, their design and fabrication still face enormous challenges. Herein, we strategically design and fabricate 1,2-dilauroyl-*sn*-glycero-3-phosphocholine-modified (DLPC-modified) bismuth nanoparticles (denoted as Bi@DLPC NPs) with desirable size of 47 ± 3 nm as a theranostic agent for photoacoustic (PA) and X-ray computed tomography (CT) imaging guided photothermal therapy (PTT) in response to near-infrared (NIR) laser irradiation. Bi@DLPC NPs possess the excellent photothermal conversion efficiency of 35% and PA/CT imaging properties, which are attributed to the strong NIR absorption and high atomic number (83) of bismuth element. Moreover, it is demonstrated that Bi@DLPC NPs are effectively accumulated in the tumor region because of the enhanced permeability and retention (EPR) effect. With the PTT, the growth of cancer cells (MDA-MB-231 cells) can be remarkably ablated in vitro and in vivo; meanwhile no obvious damage and noticeable toxicity are detected to major organs. The antitumor mechanism of Bi@DLPC NPs is attributable to the mitochondrial dysfunction and change of cell membrane permeability of MDA-MB-231 cells caused by photothermal effects upon laser irradiation. On the basis of their high stability and excellent biocompatibility, Bi@DLPC NPs have great potential for the treatment of various types of tumors.

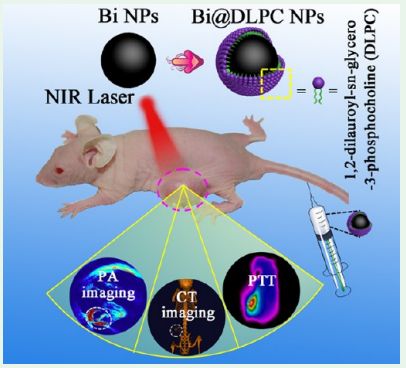


**KEYWORDS:** *theranostic agent, Bi NPs, PA imaging, CT imaging, photothermal therapy*

## INTRODUCTION

Because of its high efficiency, low invasion, and remote controllability, photothermal therapy (PTT) is regarded as one of the most promising therapeutic strategies for solid tumor ablation.[1−6] Extensive studies have been focused on PTT agents, including gold nanostructures, carbon quantum dots, copper-/bismuth-based compounds, tungsten bronzes, and various organic polymers, etc., in the past decade.[7−17] In the early stages of the PTT field, scientists mainly focused on the photothermal effect of PTT agents to kill cancer cells; however, recently considerable attention has been paid to integrate diagnosis function into PTT agents.[18,19] Cancer diagnosis mainly relies on all kinds of biological imaging methods, such as fluorescence imaging, magnetic resonance imaging (MRI), X-ray computed tomography (CT) imaging, photoacoustic (PA) imaging, positron emission tomography (PET) imaging, and so on.[20−26] A single imaging mode usually cannot meet the diagnostic requirement. PA imaging can provide more details on microstructure of a tumor site, while CT imaging has advantages in deep tissue penetration and 3D visual imaging.[27−30] The combination of PA/CT dual-imaging modalities would provide a more accurate diagnosis of cancer. Thus, the theranostic agents combining PA/CT dual-imaging with PTT functions have great potential in cancer treatment.

Most theranostic agents generally adopted the "all-in-one" strategy, which combines different functional materials into one complex nanomaterial for multiple functions. They have major drawbacks of mutual interference, complex composition, and ease of drug leakage.[31−33] On the contrary, the "one-for-all" strategy is to employ one species to achieve intrinsic multifunctionality, such as a photothermal property and multimodal imaging modalities. Currently, to the best of our knowledge, very few such theranostic agents have been reported. Hwang et al. have developed a kind of echinus-like gold nanoparticle, which possesses in vivo photodynamic and photothermal therapeutic effects in both the first (915 nm) and the second (1064 nm) near-infrared (NIR) biological windows.[34] Moreover, the $Cs_xWO_3$-based multifunctional theranostic agent has been adopted as a PA/CT dual-imaging guided PTT/PDT (PDT, photodynamic therapy) cancer dual-therapy agent.[35]

Since Bi nanoparticles (Bi NPs) are made of Bi element ($Z$ = 83) and possess good X-ray attenuation properties (Bi, 5.74; iodine, 1.94; bone, 0.186 $cm^2/g$ at 100 keV)[36−38] and strong

**Received:** November 26, 2017
**Accepted:** January 30, 2018
**Published:** January 30, 2018






DOI: 10.1021/acsanm.7b00255
ACS Appl. Nano Mater. 2018, 1, 820−830

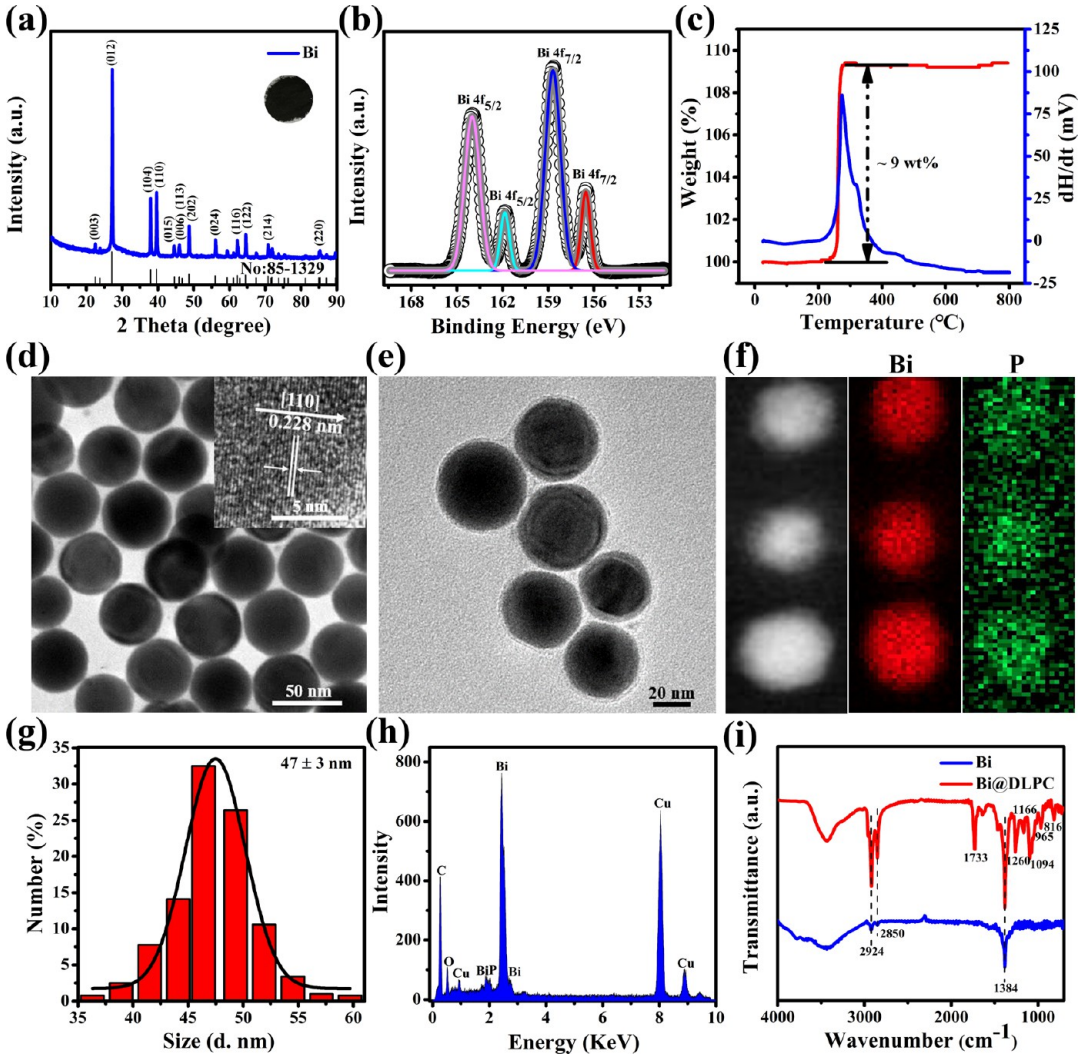


**Figure 1.** Characterizations of the as-prepared Bi NPs and Bi@DLPC NPs. (a) Powder XRD pattern and (b) XPS spectrum of Bi NPs. (c) TGA and DSC curves of Bi NPs in air atmosphere. TEM images of (d) Bi NPs and (e) Bi@DLPC NPs. Inset: HR-TEM image of Bi NPs. (f) EDS elemental mapping analysis of Bi@DLPC NPs: Bi (red) and P (green). (g) Statistical size distribution analysis of Bi@DLPC NPs ($N$ = 100). (h) EDS spectrum of Bi@DLPC NPs. (i) FT-IR spectra of Bi NPs and Bi@DLPC NPs.

absorbance in the NIR window, they are ideal theranostic agents for CT/PA imaging and PTT. However, there are few reports to date using Bi NPs as multifunctional theranostic agents for cancer treatment. Herein, we developed a novel multifunctional theranostic agent, i.e., 1,2-dilauroyl-*sn*-glycero-3-phosphocholine (DLPC) lipid-membrane-coated Bi NPs (named as Bi@DLPC NPs) for dual-imaging guided PTT, which exhibits strong optical absorbance in the NIR region and efficient tumor passive accumulation due to the enhanced permeability and retention (EPR) effect.[23,39−41] Compared with very recently published Bi-based theranostic agents,[42−44] Bi@DLPC NPs possess more biocompatibility and another potential function as a drug carrier since 1,2-dilauroyl-*sn*-glycero-3-phosphocholine (DLPC) lipid membrane was coated on the surface of Bi NPs. Hydrophobic anticancer drugs, such as paclitaxel, camptothecin, 5-fluorouracil, etc., can be embedded inside the lipid membranes.[45−47] Furthermore, Bi@DLPC NPs showed high photothermal conversion efficiency, low toxicity, and excellent water solubility. They have great potential in cancer theranostics.

## RESULTS AND DISCUSSION

**Characterizations of Bi NPs and Bi@DLPC NPs.** Monodispersed Bi NPs were prepared using oleic acid and trioctylphosphine as stabilizing and reducing agent, respectively. The procedure of the reduction reaction was very fast even within 30 s. The powder X-ray diffraction (XRD) pattern reveals that the as-obtained Bi NPs are pure Bi NPs because their characteristic peaks (Figure 1a) all match very well with those from JCPDS 85-1329 of pure Bi materials. The valence states of Bi NPs were determined by X-ray photoelectron spectroscopy (XPS) analysis. The binding energy of spin−orbit doublets Bi $4f_{7/2}$ and $4f_{5/2}$ at 156.6 and 161.9 eV in the high-resolution XPS spectrum are attributed to zerovalent Bi NPs (Figure 1b). Another two peaks at 158.7 and 164.0 eV may be due to the surface oxidation of Bi NPs in the air.[48−50] However, the surface oxidation of Bi NPs did not display any influence on their photothermal performance. Furthermore, the thermogravimetric analysis (TGA) along with differential scanning calorimetry (DSC) of noncoated samples (Bi NPs) are displayed in Figure 1c. In general, TGA curves of most inorganics modified with organics would decrease against


DOI: 10.1021/acsanm.7b00255
ACS Appl. Nano Mater. 2018, 1, 820−830

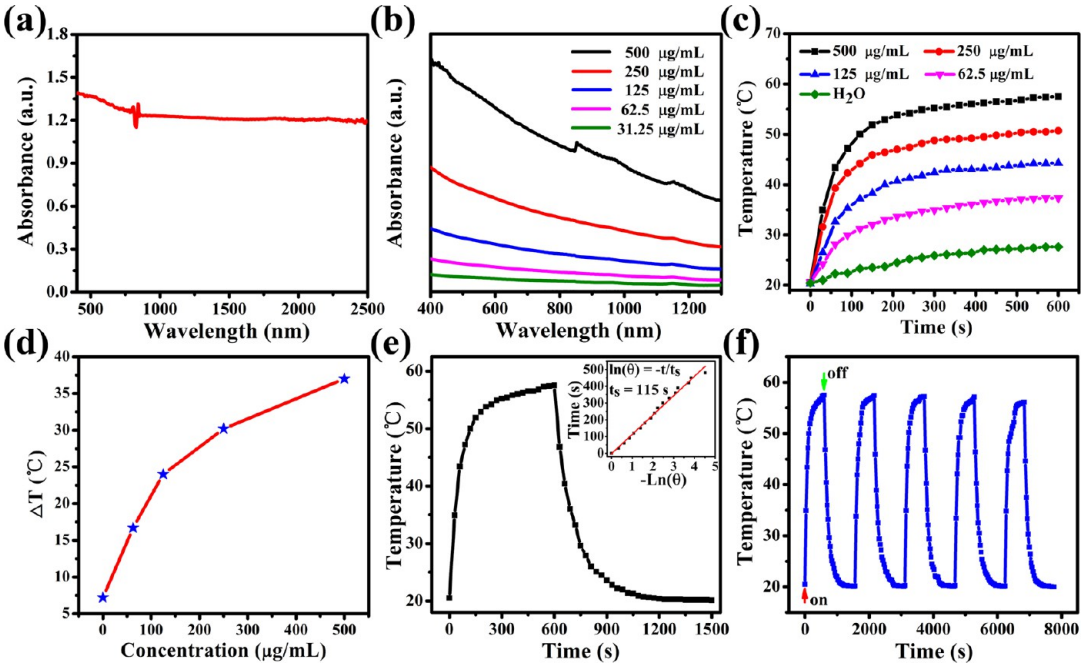


**Figure 2.** (a) UV−vis−NIR powder absorption spectrum of Bi NPs. (b) UV−vis−NIR absorption spectra of Bi@DLPC NPs dispersed in deionized water at various concentrations. (c) Photothermal heating curves of Bi@DLPC NPs at various concentrations under continuous NIR laser irradiation (880 nm, 1 W/cm$^2$) as a function of time. (d) Temperature increase ($\Delta T$) over a period of 10 min of irradiation versus the concentration of Bi@DLPC NPs. (e) Heating and cooling curves of Bi@DLPC NPs. Inset: plot of cooling time versus negative natural logarithm of the temperature driving force. (f) Photothermal stability of Bi@DLPC NPs for five laser on/off cycles.

temperature because of their decomposition and their surface organic substance. Surprisingly, in our case the weight of pure Bi NPs increases by ∼9 wt %, which originates from generation of $Bi_2O_3$. In addition, two exothermal peaks at around 273 and 322 °C on the DSC curve can be ascribed to the oxidation reaction of Bi NPs, and degradation of oleic acid and 1-dodecanethiol, respectively (Figure 1c). The high-resolution TEM (HR-TEM) image and selected-area electron diffraction (SAED) pattern indicate that the prepared nanoparticles are Bi NPs, because well-defined lattice fringes (0.228 nm; in the inset of Figure 1d) correspond to the (110) plane of Bi NPs crystal, and the SAED result contains crystal information on Bi materials (Figure S1a). The morphology and size of the as-prepared Bi NPs were determined by transmission electron microscopy (TEM), which shows relatively uniform spherical nanoparticles with an average size of 45 ± 3 nm (Figure 1d and Figure S1b). The structural composition distribution of Bi NPs was further confirmed using elemental mapping analysis by energy-dispersive X-ray spectrometry (EDS). Only Bi element is found in EDS mapping (Figure S1c). For confirmation that no $Bi_2O_3$ or BiP was formed during the synthesis, the powder XRD pattern of Bi NPs was compared with the JCPDS card of $Bi_2O_3$. From Figure S2, we can see that all the XRD peaks of the Bi NPs do not match with the XRD pattern of $Bi_2O_3$ (JCPDS 78-1793). Meanwhile, there are no P element peaks from the XPS data (Figure S3). All above-mentioned data indicate that the as-obtained Bi NPs are pure Bi NPs.

To enhance the hydrophilic property, physiological stability, and biocompatibility of Bi NPs, we employed an artificial cell membrane (DLPC membrane)[51,52] to modify Bi NPs by an ultrasonic method. As shown in Figure 1e, it is noted that Bi@DLPC NPs are also in spherical shape with average diameter of 47 ± 3 nm (Figure 1g). The diameter difference of 2 nm between Bi@DLPC NPs and Bi NPs is consistence with the thickness of the DLPC monolayer. The existence of phosphorus (P) element in the EDS mapping (Figure 1f) and EDS spectrum (Figure 1h) confirms the successful coating of DLPC membrane outside of Bi NPs. The average hydrodynamic size of Bi@DLPC NPs (162 nm; Figure S4) is larger than that from TEM. This kind of difference is also found in reported results.[53,54] The polydispersity index (PDI) of Bi@DLPC NPs in water is 0.129, suggesting the excellent monodispersity of Bi@DLPC NPs. The average hydrodynamic size of Bi@DLPC NPs fulfills the requirement of the EPR effect for tumor treatment. The Fourier transform infrared (FT-IR) spectra of Bi NPs and Bi@DLPC NPs were measured to further verify successful coating of DLPC. As illustrated in Figure 1i, the peaks at 1384, 2850, and 2924 cm$^{-1}$ are associated with the deformation vibration bands of $CH_3$, and C—H stretching vibrations for surface organic components of the as-prepared Bi NPs, respectively. After coating with DLPC, a prominent band at 1260 cm$^{-1}$ corresponding to the P═O stretching vibration of DLPC is found. Other new peaks can be assigned to the C═O deformation vibration (1733 cm$^{-1}$), C—O—C stretching vibration (1166 cm$^{-1}$), C—N stretching vibration (1094 cm$^{-1}$), C—O stretching vibration of P—O—C (965 cm$^{-1}$), and P—O stretching vibration of P—O—C (816 cm$^{-1}$), respectively. Those peaks confirm the successful modification of DLPC on Bi NPs. In addition, the TGA along with DSC of coated samples (Bi@DLPC NPs) are displayed in Figure S5. As illustrated in Figure S5, the weight loss of Bi@DLPC NPs is ∼12 wt % due to the degradation of DLPC, oleic acid, and 1-dodecanethiol, which appeared in the exothermal peaks at around 294 and 318 °C on the DSC curve, respectively.

**Optical and Photothermal (PT) Properties of Bi@DLPC NPs.** The ultraviolet−visible−near-infrared (UV−vis−NIR) absorption spectrum of powder Bi NPs (Figure 2a) exhibits


DOI: 10.1021/acsanm.7b00255
ACS Appl. Nano Mater. 2018, 1, 820−830

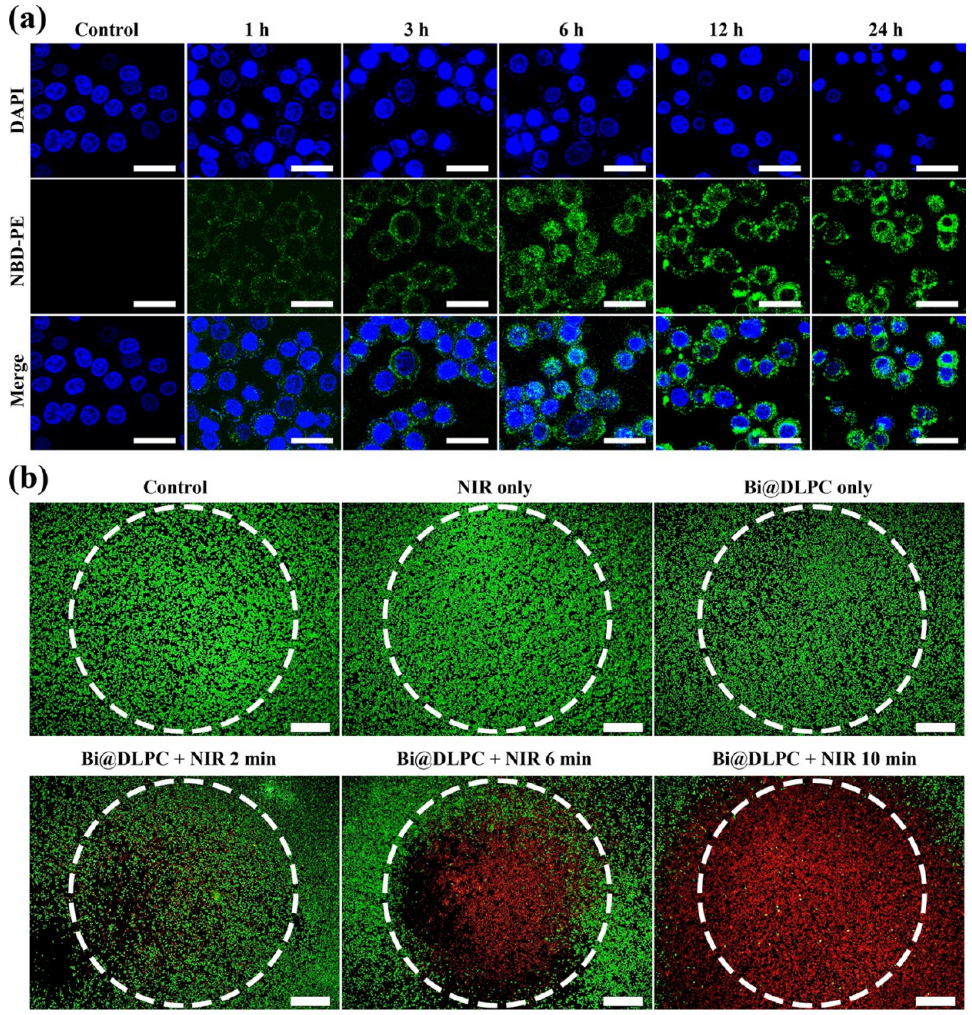


**Figure 3.** (a) Confocal microscopy images of MDA-MB-231 treated with NBD PE-labeled Bi@DLPC NPs for different times. Nuclei were stained with DAPI (scale bars, 25 $\mu$m). (b) Fluorescence images of calcein-AM and PI costaining to visualize MDA-MB-231 cells treated with different conditions (scale bars, 500 $\mu$m).

strong full spectrum adsorption from 400 to 2500 nm, which implies that they are a potential photothermal agent under NIR laser irradiation. The UV−vis−NIR absorption spectra of Bi@DLPC NPs solutions with different concentrations (Figure 2b) show remarkable concentration-dependent absorbance (Figure S6) from the visible to NIR region, indicating that Bi@DLPC NPs are good candidates for photothermal therapy (PTT). The unusual peaks in Figure 2a,b are due to the change of light source inside the instruments and are inevitable (Hitachi). Moreover, the as-prepared Bi@DLPC NPs exhibit excellent dispersibility and stability in different solvents including deionized water, phosphate buffered saline (PBS), Dulbecco's modified Eagle's medium (DMEM), and fetal bovine serum (FBS), separately (Figure S7). For an investigation of the NIR laser-induced photothermal therapy (PTT) effect, Bi@DLPC NPs with various concentrations (0−500 $\mu$g/mL) were continuously irradiated using an NIR laser at 880 nm with a safe power density of 1 W/cm$^2$ for 10 min. Figure 2c,d distinctly reveals a concentration-dependent photothermal property of Bi@DLPC NPs. The temperature of the Bi@DLPC NP solution (500 $\mu$g/mL) greatly increases by 37 °C after irradiation of 10 min, while the temperature of the deionized water only increases by 7.2 °C at the same conditions. The photothermal conversion efficiency ($\eta$) of Bi@DLPC NPs was calculated to be 35% according to a previously reported method (Figure 2e).[55] Moreover, the photothermal stability of Bi@DLPC NPs was investigated by irradiating them for 10 min followed by naturally cooling to room temperature for 15 min as one cycle. Five repeats only display a 3% decrease in photothermal stability (Figure 2f), which indicates preferable photothermal stability compared with organic dyes.[41]

**In Vitro Cellular Uptake, Cytotoxicity, and Antitumor Effect of Bi@DLPC NPs.** The cellular uptake of Bi@DLPC NPs is of key importance to evaluate their anticancer therapy property. Therefore, the cellular uptake and internalization distribution of Bi@DLPC NPs (containing fluorescent-labeled NBD PE) were investigated using MDA-MB-231 cells (breast cancer cells) by confocal laser scanning microscopy (CLSM). The NBD PE-labeled Bi@DLPC NPs exhibit a time-dependent cellular uptake behavior (Figure 3a). The blue area in Figure 3a represents the nucleus of MDA-MB-231 cells, while the green dots are Bi@DLPC NPs. The bottom row images are the merged images of top row and middle row in the same columns. It is noted that the green dots accumulate more and more around nuclei against time. In addition, we further compared the cellular uptake abilities of Bi NPs with different surface modifications. First, we modified the Bi NPs with


DOI: 10.1021/acsanm.7b00255
ACS Appl. Nano Mater. 2018, 1, 820−830

DLPC, DSPE-PEG-2000, and PVP, separately. All the samples show excellent dispersibility in water (Figure S8a) and relatively uniform spherical shape (Figure S8b–d) after different modifications. To validate the successful surface modifications, we monitored the FT-IR spectra of the three samples. We have already confirmed the successful modification of DLPC on Bi NPs (Figure 1i and Figure S8e). The FT-IR spectra in Figure S8f show a characteristic absorption peak at 1105 $cm^{-1}$ corresponding to the C—O stretching vibration of DSPE-PEG-2000 after coating with DSPE-PEG-2000. The peaks at 2917 and 2849 $cm^{-1}$ are associated with the deformation vibration bands of C—H stretching vibrations for surface organic components of DSPE-PEG-2000, confirming the successful modification of DSPE-PEG-2000 on Bi NPs. As can be seen in Figure S8g, the peaks at 2922 and 2842 $cm^{-1}$ are associated with the deformation vibration bands of C—H stretching vibrations for surface organic components of PVP. Meanwhile, the bands at 1675 and 1284 $cm^{-1}$ are assigned to C═O and C—N stretching vibrations of PVP, which demonstrated the successful modification of PVP on Bi NPs. Next, we explored and compared the cellular uptake abilities of Bi@DLPC, Bi@DSPE-PEG-2000, and Bi@PVP NPs. MDA-MB-231 cells were incubated with the three samples for 24 h and lysed in the digesting solution. The contents of Bi in the MDA-MB-231 cells were determined by inductively coupled plasma optical emission spectrometry (ICP-OES) analysis. As can be seen in Figure S8h, the cellular uptake abilities show the order of Bi@DLPC > Bi@DSPE-PEG-2000 > Bi@PVP NPs with different concentrations. The results indicated that the Bi@DLPC NPs possessed higher cellular uptake ability than the Bi@DSPE-PEG-2000 and Bi@PVP NPs at the same concentration and incubation time.

The investigation of the cytotoxicity of a novel theranostic agent is of significance for determining its potential in the anticancer field. Since the uncoated Bi NPs are hydrophobic, the cytotoxicity of noncoated Bi NPs is impossible to be analyzed. Lipid coating on Bi NPs enables them to be soluble in aqueous solution. Therefore, we evaluated the potential cytotoxicity of Bi@DLPC NPs toward MDA-MB-231 and MCF-10A cells (breast epithelial cells) for 24 h using 3-(4,5-dimethylthialzol-2-yl)-2,5-diphenyltetrazolium bromide (MTT) assay (Figure S9). As expected, MTT results show a negligible cytotoxicity for Bi@DLPC NPs with concentration below 250 $\mu$g/mL, and 87% cell viability with 500 $\mu$g/mL of Bi@DLPC NPs, which indicates the low cytotoxicity of Bi@DLPC NPs.

The remarkable photothermal stability and excellent photothermal conversion performance of Bi@DLPC NPs enable them to be good photothermal agents. Hence, the in vitro antitumor performance of Bi@DLPC NPs toward MDA-MB-231 cells was investigated using a fluorescent microscope. The live cells and dead cells were stained with calcein-AM (green) and PI (red), respectively. There is no cancer cell death upon the conditions of both NIR laser irradiation only (10 min, 880 nm, 1 W/$cm^2$) and Bi@DLPC NPs only (Figure 3b). However, the amount of dead cells increased with NIR laser irradiation time together with 250 $\mu$g/mL of Bi@DLPC NPs (Figure 3b). The above-mentioned results confirm the excellent photothermal performance of Bi@DLPC NPs toward cancer cell treatment. The antitumor mechanism is probably due to the permeability change of cell membrane and the damage of mitochondria. The ethidium bromide (EB) molecule is membrane-impermeable, and exhibits red fluorescence after binding with nucleic acid.[41,56] MDA-MB-231 cells treated with Bi@DLPC NPs exhibit intensely red fluorescence under NIR laser irradiation because EB molecules effectively enter into apoptotic/dead cells from the damaged membrane and react with nucleic acids (Figure S10, bottom right image). However, we did not observe the EB molecules inside the cells in the experimental conditions of control, NIR laser irradiation only, and Bi@DLPC NPs only. These results suggest that Bi@DLPC NPs combined with NIR laser irradiation can effectively lead to a cell membrane permeability change by hyperthermia. The mitochondria were also damaged during the PTT treatment. It is well-known that JC-1 indicator is a mitochondrial probe to assess function of the mitochondria.[41] With the normal mitochondria, JC-1 molecules form aggregates to display red fluorescence, while with damaged mitochondria, JC-1 molecules exist as monomers to show green fluorescence. From the images in the bottom row of Figure 4, it is clearly seen that the mitochondria are damaged with 250 $\mu$g/mL of Bi@DLPC NPs under 10 min of NIR laser irradiation. In contrast, for cells treated with NIR laser irradiation only, the Bi@DLPC NPs only group still retains the same red fluorescence with normal cells (control), which indicates that the mitochondria are not damaged under those experimental conditions. These results suggest that the dysfunction of mitochondria under NIR laser-induced PTT may be one of the reasons causing cell apoptosis.

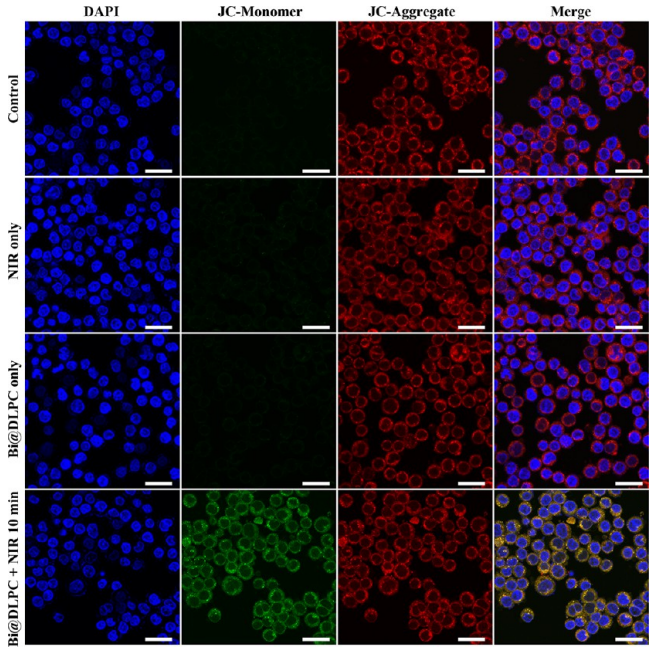


**Figure 4.** Mitochondrial membrane potential change study of MDA-MB-231 cells with JC-1 staining after different treatments: control, NIR laser irradiation only, Bi@DLPC NPs only, and Bi@DLPC NPs with NIR laser irradiation (880 nm, 1 W/$cm^2$) for 10 min (scale bar, 25 $\mu$m).

**In Vitro and in Vivo PA/CT Imaging of Bi@DLPC NPs.** Ideal multifunctional theranostic agents should possess both excellent therapy and remarkable imaging contrast effects. Bi@DLPC NPs were found to be ideal photoacoustic (PA) and CT imaging contrast agents. PA imaging with high spatial resolution and deep penetration ability is a new emerging biomedical imaging technique to provide bioinformation for tumor tissue structures.[57] Figure S11a and Figure 5a exhibit a gradually enhanced PA signal intensity for Bi@DLPC NPs with


DOI: 10.1021/acsanm.7b00255
ACS Appl. Nano Mater. 2018, 1, 820–830

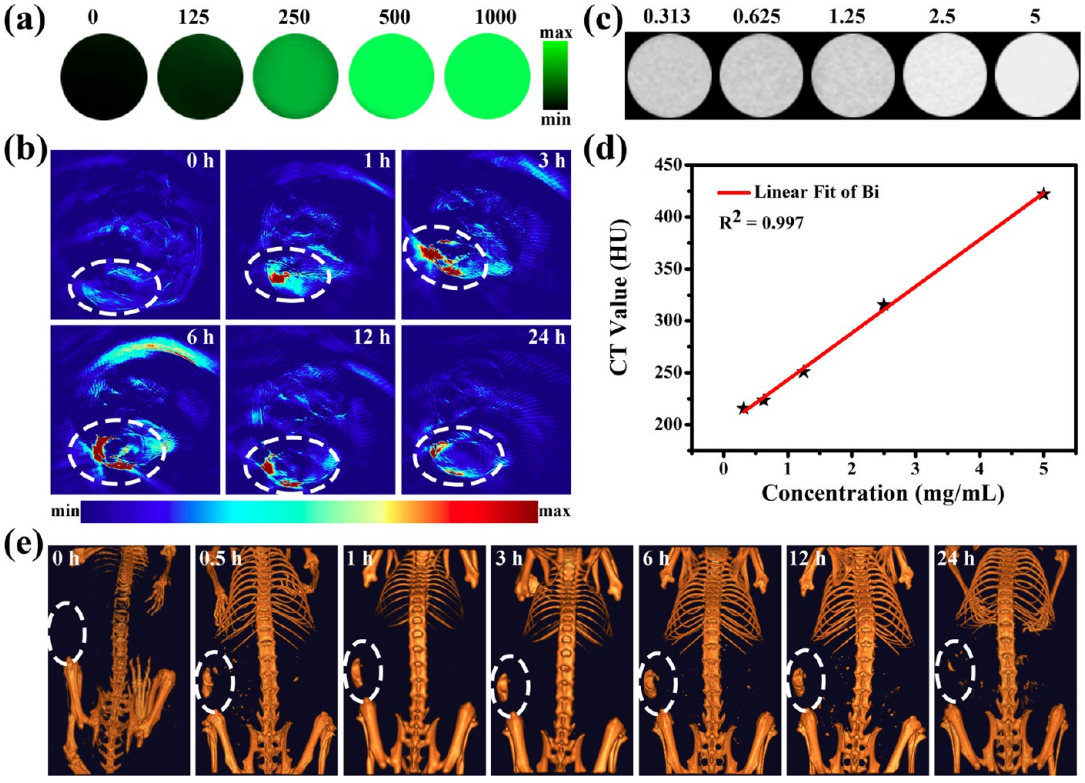


**Figure 5.** In vitro and in vivo PA and CT imaging. (a) PA images of Bi@DLPC NPs as a function of concentration ($\mu$g/mL). (b) In vivo PA imaging of MDA-MB-231 tumor-bearing mice after intravenously injection of Bi@DLPC NPs (2 mg/mL, 100 $\mu$L) at different times (0, 1, 3, 6, 12, 24 h). (c) In vitro CT images (mg/mL) and (d) HU values of Bi@DLPC NPs at various concentrations. (e) In vivo CT imaging of MDA-MB-231 tumor-bearing mice after intratumoral injection of Bi@DLPC NPs (4 mg/mL, 100 $\mu$L) at different times (0, 0.5, 1, 3, 6, 12, 24 h).

concentration from 0 to 1000 $\mu$g/mL. The calibration curve at 880 nm in Figure S11b indicates the concentration-dependent property of Bi@DLPC NPs as PA imaging agents. Bi@DLPC NPs (2 mg/mL, 100 $\mu$L) were then intravenously injected into MDA-MB-231 tumor-bearing mice to achieve PA signals in vivo under 880 nm excitation laser at different times (0, 1, 3, 6, 12, 24 h), as shown in Figure 5b. Only a weak PA signal in tumor sites (circle area in the image) is observed before injection of Bi@DLPC NPs due to the existence of oxyhemoglobin and deoxyhemoglobin in the tumor vasculatures. The signals become more and more pronounced from 1 to 6 h after injection due to the EPR effect benefiting from the suitable size (162 nm) of Bi@DLPC NPs. These results illustrate that Bi@DLPC NPs can effectively accumulate at tumor sites by long-time circulation in vasculatures. From 6 to 24 h, the PA signals gradually decrease. It is concluded that the accumulative amount of Bi@DLPC NPs peaks at 6 h after injection. Therefore, in the following in vivo tumor treatment, 6 h after injection is chosen to start PTT treatment. Bi@DLPC NPs with a high X-ray attenuation ability due to the large Bi atomic number ($Z$ = 83) are expected to be CT imaging contrast agents. The CT imaging property of Bi@DLPC NPs was investigated using a computed X-ray tomography scanner. With the increase of Bi@DLPC NP concentrations, the signal intensity of each corresponding CT image remarkably enhances (Figure 5c). The Hounsfield unit (HU) values of Bi@DLPC NPs in vitro present a concentration-dependent linear behavior with the slope of HU value to be 45 HU L/g (Figure 5d). Before administration of Bi@DLPC NPs, no CT signal was observed in the tumor region. Particularly, after the MDA-MB-231 tumor-bearing mice were intratumorally administrated with 100 $\mu$L of Bi@DLPC NPs (4 mg/mL), remarkable CT signals from Bi@DLPC NPs at the tumor region were clearly observed, which displayed a long-time CT imaging ability even after intratumoral injection for 12 h. Therefore, Bi@DLPC NPs are confirmed to be excellent contrast agents for CT imaging (Figure 5e).

**In Vivo Antitumor Efficacy, Blood Biochemistry Analysis, and Biodistribution of Bi@DLPC NPs.** Encouraged by the excellent biocompatibility, high photothermal conversion efficiency ($\eta$), and antitumor efficacy in vitro of Bi@DLPC NPs, we further evaluated their antitumor efficacy in vivo. MDA-MB-231 tumor-bearing mice with an approximate volume of 200 mm$^3$ were randomly assigned to five groups (5 mice in each group), including PBS injection only as a control group I, NIR laser irradiation only as group II, Bi@DLPC NPs injection only as group III, Bi@DLPC NPs injection plus NIR laser irradiation for 5 min as group IV, and 10 min as group V, respectively. The mice were intravenously administrated with 100 $\mu$L of PBS or Bi@DLPC NPs (1 mg/mL), and then irradiated by NIR laser (880 nm, 1 W/cm$^2$) at 6 h postinjection. The infrared thermal camera was employed to take infrared thermal images and monitor temperature change of the tumor area under NIR laser irradiation (Figure 6a,b). The results show that the surface temperature of the tumor area in the mouse injected with Bi@DLPC NPs dramatically increases from 37.4 to 57.7 °C by NIR laser irradiation for 10 min. On the contrary, the temperature of the tumor area of the mouse treated with NIR laser irradiation only (group II) only increases to 43.8 °C (Figure 6b). These data confirm the efficient NIR energy absorption of Bi@DLPC NPs in vivo to ablate tumors. The relative volume changes of tumors of groups


DOI: 10.1021/acsanm.7b00255
ACS Appl. Nano Mater. 2018, 1, 820−830

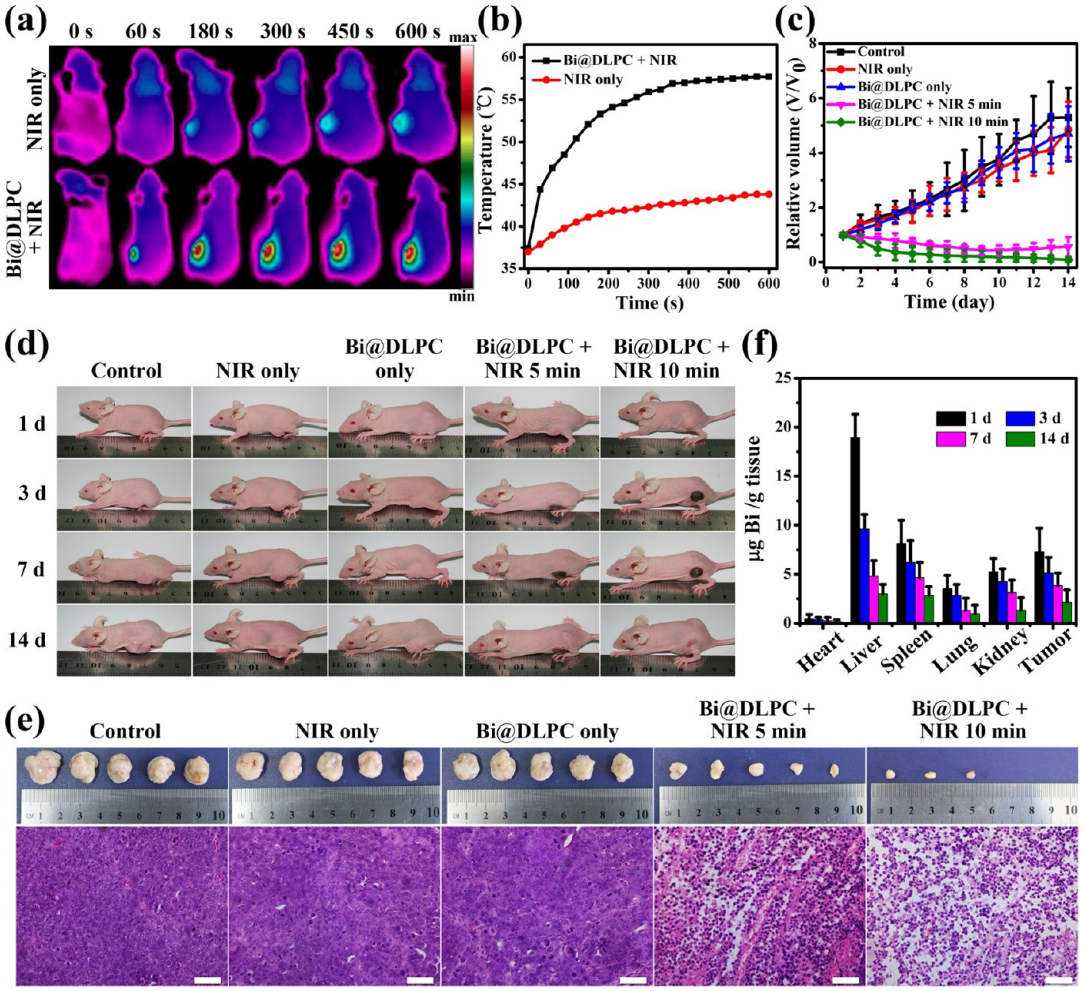


**Figure 6.** In vivo antitumor efficacy of Bi@DLPC NPs. (a) Infrared thermal images and (b) temperature curves against time in the tumor site of MDA-MB-231 tumor-bearing mice intravenously injected with Bi@DLPC NPs (1 mg/mL, 100 $\mu$L) at 6 h under NIR laser irradiation (1 W/cm$^2$). (c) Normalized tumor volumes during the therapeutic period after different treatments. (d) Representative photos of mice from each experimental group during the treatments. (e) Photographs and their corresponding hematoxylin and eosin (H&E) staining of tumor tissues at the 14th day after different treatments (scale bar, 50 $\mu$m). (f) Biodistribution of Bi@DLPC NPs in major organs of mice after intravenous injection for different times ($n$ = 3).

I–V were monitored by caliper during the subsequent 14 days (Figure 6c). The tumor volumes of NIR laser irradiation only (group II) and Bi@DLPC NPs injection only (group III) exhibit a slight decrease compared with the control group (group I) as expected. Interestingly, tumor size of Bi@DLPC NPs combined with NIR laser irradiation for 5 min (group IV) decreases in the first 9 days, but reverses during the following 5 days (pink curve in Figure 6c). The hyperthermia in this case is not enough for the whole tumor ablation. When the irradiation time increased to 10 min, the hyperthermia caused by Bi@DLPC NPs led to an effective tumor ablation because the tumors of two mice were even cured after the treatment (Figure 6c–e). For further confirmation of the PTT efficacy of Bi@DLPC NPs, hematoxylin and eosin (H&E) were used to stain tumor tissues in different groups as shown in the bottom images of Figure 6e. There is no significant damage to tumor cells for groups I, II, and III. However, the partial cell necrosis for group IV and relative high cell necrosis ratio for group V are observed.

The biodistribution of Bi@DLPC NPs is also important in biomedical fields. Therefore, the distributions of bismuth (Bi) in the major organs (heart, liver, spleen, lung, and kidney) of mice and tumors at 1, 3, 7, and 14 days were analyzed by ICP-OES measurement, as shown in Figure 6f. Bi@DLPC NPs mainly distribute in the liver and spleen because of the filtering effect of the reticuloendothelial system (RES).[58,59] Bi@DLPC NPs accumulated in major organs could be remarkably decreased from the 1st day to the 14th day, indicating that they show a time-dependent clearance effect. Previous studies indicated that the liver is the most effective elimination pathway for nanoparticles because Kupffer cells in the liver can quickly phagocytize the nanoparticles.[60] The energy required of phagocytosis is obtained by glycolysis; thus a large amount of lactic acid will be produced and accumulated in the liver. Meanwhile, the pH value in the phagosome can reach ~4. If the nanoparticles accumulated in the liver, they will react with glucuronic acid and sulfuric acid in the liver. Thus, we studied the possible metabolic mechanism of Bi@DLPC NPs by simulating the liver environment in vitro. The simulated liver liquid was configured by adding 10 $\mu$L of 0.5 M glucuronic acid, 1 M lactic acid, and 1 M sulfuric acid in a beaker, and then, the deionized water was added into the beaker and was followed by adjusting the pH to ~4. Bi@DLPC NPs were added into five different bottles, which contained 4 mL of simulated liver


DOI: 10.1021/acsanm.7b00255
ACS Appl. Nano Mater. 2018, 1, 820–830

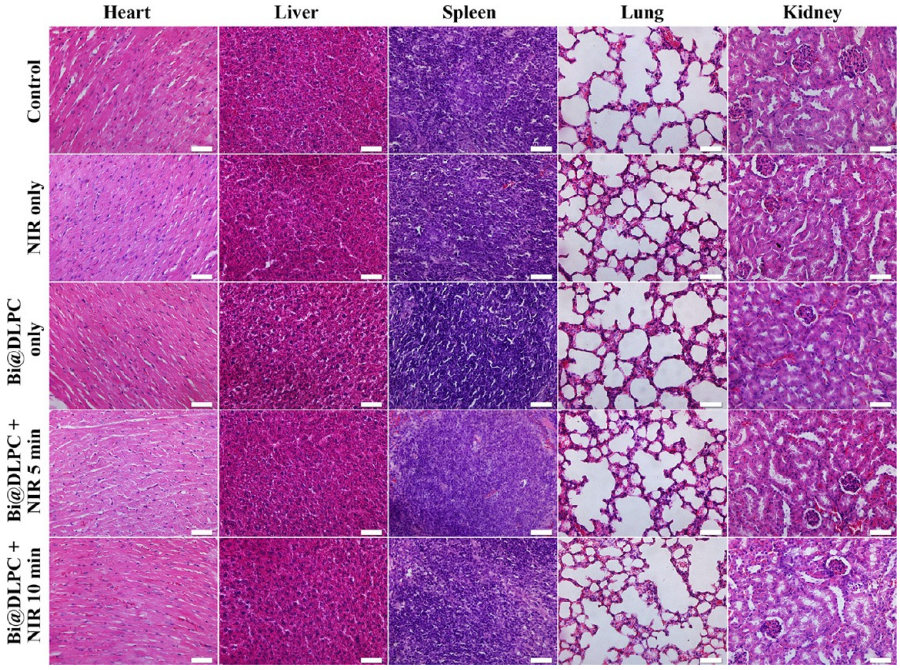


**Figure 7.** Histology analysis of mice major organs (heart, liver, spleen, lung, kidney) at the 14th day after different treatments (scale bar, 50 $\mu$m).

liquid. The concentration of Bi@DLPC NPs in each bottle is 50 mg/L. The five bottles were stirred by magnetic force for 0, 1, 3, 7, and 14 days, and then centrifuged to obtain the supernatants. The concentration of $Bi^{3+}$ in each supernatant was tested by ICP-OES. As can be seen in Figure S12, we can see the free $Bi^{3+}$ remarkably increased from the 1st day to the 14th day, indicating the degradation of Bi@DLPC NPs. To the best of our knowledge, it is important to know the blood circulation situation of Bi@DLPC NPs. The concentration of Bi@DLPC NPs in blood was calculated to be 38.3% at 24 h according to the distributional data (ICP) of Bi@DLPC NPs in different organs. In addition, we also know that Bi@DLPC NPs can accumulate very well in the tumor site by the blood circulation from PA imaging in vivo, which indicated the good blood circulation ability of Bi@DLPC NPs.

Because the biological toxicity of a novel material has to be carefully evaluated before its potential application in the clinical setting, we measured biological toxicity of Bi@DLPC NPs in vivo by body weight changes, H&E staining, and blood analysis. The body weight changes among these groups show negligible difference within 14 days (Figure S13). As expected, no remarkable damage (i.e., necrosis or inflammation) is revealed for the major organs, including heart, liver, spleen, lung, and kidney of all mice (Figure 7). For the blood biochemistry analysis, all kinds of representative hematology indicators of the treated mice were analyzed, including red blood cell (RBC), white blood cell (WBC), hemoglobin (HGB), hematocrit (HCT), platelet (PLT), mean corpuscular volume (MCV), mean corpuscular hemoglobin (MCH), and mean corpuscular hemoglobin concentration (MCHC), separately. It is noted that all indicators are within normal ranges (Figure S14). All above-mentioned results indicate that Bi@DLPC NPs are of low biological toxicity during the tumor treatment.

## CONCLUSION

In summary, we fabricated a novel "one-for-all" multimodal imaging (PA/CT) guided photothermal theranostic agent, i.e., DLPC-membrane-coated Bi NPs. Bi@DLPC NPs exhibited superior photothermal conversion efficiency, PA/CT imaging contrast, photostability, biocompatibility, excellent cellular uptake efficiency, and passive tumor accumulation via EPR effect. Cancer cells were efficiently ablated in vitro and in vivo by Bi@DLPC NPs combined with NIR light irradiation. Their antitumor mechanism was attributed to the change of cell membrane permeability and mitochondrial dysfunction. The hematology and histology analysis results of Bi@DLPC NPs further certify their potential for in vivo application. Therefore, Bi@DLPC NPs are a potential multifunctional theranostic nanoplatform for cancer treatment in clinical trials and pave the way to use single matter for multifunctional theranostics.

## ASSOCIATED CONTENT

### Supporting Information

The Supporting Information is available free of charge on the ACS Publications website at DOI: 10.1021/acsanm.7b00255.

Additional experimental details, photothermal conversion efficiency calculation, and figures including SAED pattern, statistical size distribution analysis, EDS elemental mapping analysis, powder XRD pattern, XPS survey spectra, DLS analysis, TGA and DSC curves, absorbance vs concentration, photographs, TEM images, FT-IR spectra, cell viability assay, permeability study, PA signal intensity vs concentration, and blood biochemistry analysis (PDF)

## AUTHOR INFORMATION

### Corresponding Authors

*E-mail: shaoqinliu@hit.edu.cn.
*E-mail: hanxiaojun@hit.edu.cn.

### ORCID

Chongshen Guo: 0000-0002-8000-7434
Wei Guo: 0000-0001-5445-7872
Shaoqin Liu: 0000-0001-6990-8728



DOI: 10.1021/acsanm.7b00255
ACS Appl. Nano Mater. 2018, 1, 820−830

Xiaojun Han: 0000-0001-8571-6187

### Author Contributions

[§]C.Y. and C.G. contributed equally.

### Notes

The authors declare no competing financial interest.

## ■ ACKNOWLEDGMENTS

This work was financially supported by the National Natural Science Foundation of China (Grant 21773050, 21528501), and the Open Funds of the State Key Laboratory of Electroanalytical Chemistry (SKLEAC201707).

## ■ REFERENCES

(1) Liu, T.; Shi, S. X.; Liang, C.; Shen, S. D.; Cheng, L.; Wang, C.; Song, X. J.; Goel, S.; Barnhart, T. E.; Cai, W. B.; Liu, Z. Iron Oxide Decorated $MoS_2$ Nanosheets with Double PEGylation for Chelator-Free Radiolabeling and Multimodal Imaging Guided Photothermal Therapy. *ACS Nano* **2015**, *9*, 950−960.

(2) Xiao, Q. F.; Zheng, X. P.; Bu, W. B.; Ge, W. Q.; Zhang, S. J.; Chen, F.; Xing, H. Y.; Ren, Q. G.; Fan, W. P.; Zhao, K. L.; Hua, Y. Q.; Shi, J. L. A Core/Satellite Multifunctional Nanotheranostic for in Vivo Imaging and Tumor Eradication by Radiation/Photothermal Synergistic Therapy. *J. Am. Chem. Soc.* **2013**, *135*, 13041−13048.

(3) Liang, C.; Diao, S.; Wang, C.; Gong, H.; Liu, T.; Hong, G. S.; Shi, X. Z.; Dai, H. J.; Liu, Z. Tumor Metastasis Inhibition by Imaging-Guided Photothermal Therapy with Single-Walled Carbon Nanotubes. *Adv. Mater.* **2014**, *26*, 5646−5652.

(4) Cheng, L.; Wang, C.; Feng, L. Z.; Yang, K.; Liu, Z. Functional Nanomaterials for Phototherapies of Cancer. *Chem. Rev.* **2014**, *114*, 10869−10939.

(5) Shibu, E. S.; Hamada, M.; Murase, N.; Biju, V. Nanomaterials Formulations for Photothermal and Photodynamic Therapy of Cancer. *J. Photochem. Photobiol., C* **2013**, *15*, 53−72.

(6) Peng, J. J.; Zhao, L. Z.; Zhu, X. J.; Sun, Y.; Feng, W.; Gao, Y. H.; Wang, L. Y.; Li, F. Y. Hollow Silica Nanoparticles Loaded with Hydrophobic Phthalocyanine for Near-Infrared Photodynamic and Photothermal Combination Therapy. *Biomaterials* **2013**, *34*, 7905−7912.

(7) Pan, L. M.; Liu, J. N.; Shi, J. L. Nuclear-Targeting Gold Nanorods for Extremely Low NIR Activated Photothermal Therapy. *ACS Appl. Mater. Interfaces* **2017**, *9*, 15952−15961.

(8) Zhao, X.; Yang, C. X.; Chen, L. G.; Yan, X. P. Dual-Stimuli Responsive and Reversibly Activatable Theranostic Nanoprobe for Precision Tumor-Targeting and Fluorescence-Guided Photothermal Therapy. *Nat. Commun.* **2017**, *8*, 14998.

(9) Wang, H.; Revia, R.; Wang, K.; Kant, R. J.; Mu, Q. X.; Gai, Z.; Hong, K. L.; Zhang, M. Q. Paramagnetic Properties of Metal-Free Boron-Doped Graphene Quantum Dots and Their Application for Safe Magnetic Resonance Imaging. *Adv. Mater.* **2017**, *29*, 1605416.

(10) Liu, X. L.; Jiang, H.; Ye, J.; Zhao, C. Q.; Gao, S. P.; Wu, C. Y.; Li, C. H.; Li, J. C.; Wang, X. M. Nitrogen-Doped Carbon Quantum Dot Stabilized Magnetic Iron Oxide Nanoprobe for Fluorescence, Magnetic Resonance, and Computed Tomography Triple-Modal in Vivo Bioimaging. *Adv. Funct. Mater.* **2016**, *26*, 8694−8706.

(11) Li, B.; Yuan, F. K.; He, G. J.; Han, X. Y.; Wang, X.; Qin, J. B.; Guo, Z. X.; Lu, X. W.; Wang, Q.; Parkin, I. P.; Wu, C. T. Ultrasmall $CuCo_2S_4$ Nanocrystals: All-in-One Theragnosis Nanoplatform with Magnetic Resonance/Near-Infrared Imaging for Efficiently Photothermal Therapy of Tumors. *Adv. Funct. Mater.* **2017**, *27*, 1606218.

(12) Li, Z. G.; Liu, J.; Hu, Y.; Howard, K. A.; Li, Z.; Fan, X. L.; Chang, M. L.; Sun, Y.; Besenbacher, H.; Chen, C. Y.; Yu, M. Multimodal Imaging-Guided Antitumor Photothermal Therapy and Drug Delivery Using Bismuth Selenide Spherical Sponge. *ACS Nano* **2016**, *10*, 9646−9658.

(13) Dou, R. X.; Du, Z.; Bao, T.; Dong, X. H.; Zheng, X. P.; Yu, M.; Yin, W. Y.; Dong, B. B.; Yan, L.; Gu, Z. J. The Polyvinylpyrrolidone Functionalized rGO/$Bi_2S_3$ Nanocomposite as a Near-Infrared Light-Responsive Nanovehicle for Chemo-Photothermal Therapy of Cancer. *Nanoscale* **2016**, *8*, 11531−11542.

(14) Xie, H. H.; Li, Z. B.; Sun, Z. B.; Shao, J. D.; Yu, X. F.; Guo, Z. N.; Wang, J. H.; Xiao, Q. L.; Wang, H. Y.; Wang, Q. Q.; Zhang, H.; Chu, P. K. Metabolizable Ultrathin $Bi_2Se_3$ Nanosheets in Imaging-Guided Photothermal Therapy. *Small* **2016**, *12*, 4136−4145.

(15) Guo, C. S.; Yu, H. J.; Feng, B.; Gao, W. D.; Yan, M.; Zhang, Z. W.; Li, Y. P.; Liu, S. Q. Highly Efficient Ablation of Metastatic Breast Cancer Using Ammonium-Tungsten-Bronze Nanocube as a Novel 1064 nm-Laser-Driven Photothermal Agent. *Biomaterials* **2015**, *52*, 407−416.

(16) Guo, C. S.; Yin, S.; Yu, H. J.; Liu, S. Q.; Dong, Q.; Goto, T.; Zhang, Z. W.; Li, Y. P.; Sato, T. Photothermal Ablation Cancer Therapy Using Homogeneous $Cs_xWO_3$ Nanorods with Broad Near-Infrared Absorption. *Nanoscale* **2013**, *5*, 6469−6478.

(17) Li, F.; Li, T.; Cao, W.; Wang, L.; Xu, H. P. Near-Infrared Light Stimuli-Responsive Synergistic Therapy Nanoplatforms Based on the Coordination of Tellurium-Containing Block Polymer and Cisplatin for Cancer Treatment. *Biomaterials* **2017**, *133*, 208−218.

(18) Chen, W. R.; Adams, R. L.; Higgins, A. K.; Bartels, K. E.; Nordquist, R. E. Photothermal Effects on Murine Mammary Tumors Using Indocyanine Green and an 808-nm Diode Laser: An in Vivo Efficacy Study. *Cancer Lett.* **1996**, *98*, 169−173.

(19) Guo, W.; Qiu, Z. Y.; Guo, C. S.; Ding, D. D.; Li, T. C.; Wang, F.; Sun, J. Z.; Zheng, N. N.; Liu, S. Q. Multifunctional Theranostic Agent of $Cu_2(OH)PO_4$ Quantum Dots for Photoacoustic Image-Guided Photothermal/Photodynamic Combination Cancer Therapy. *ACS Appl. Mater. Interfaces* **2017**, *9*, 9348−9358.

(20) Zhang, B.; Wang, H. F.; Shen, S.; She, X. J.; Shi, W.; Chen, J.; Zhang, Q. Z.; Hu, Y.; Pang, Z. Q.; Jiang, X. G. Fibrin-Targeting Peptide CREKA-Conjugated Multi-Walled Carbon Nanotubes for Self-Amplified Photothermal Therapy of Tumor. *Biomaterials* **2016**, *79*, 46−55.

(21) Song, X. J.; Gong, H.; Liu, T.; Cheng, L.; Wang, C.; Sun, X. Q.; Liang, C.; Liu, Z. J-Aggregates of Organic Dye Molecules Complexed with Iron Oxide Nanoparticles for Imaging-Guided Photothermal Therapy Under 915-nm Light. *Small* **2014**, *10*, 4362−4370.

(22) Ding, X.; Liow, C. H.; Zhang, M.; Huang, R.; Li, C.; Shen, H.; Liu, M.; Zou, Y.; Gao, N.; Zhang, Z.; Li, Y.; Wang, Q.; Li, S.; Jiang, J. Surface Plasmon Resonance Enhanced Light Absorption and Photothermal Therapy in the Second Near-Infrared Window. *J. Am. Chem. Soc.* **2014**, *136*, 15684−15693.

(23) Zhang, S. H.; Sun, C. X.; Zeng, J. F.; Sun, Q.; Wang, G. L.; Wang, Y.; Wu, Y.; Dou, S. X.; Gao, M. Y.; Li, Z. Ambient Aqueous Synthesis of Ultrasmall PEGylated $Cu_{2-x}Se$ Nanoparticles as a Multifunctional Theranostic Agent for Multimodal Imaging Guided Photothermal Therapy of Cancer. *Adv. Mater.* **2016**, *28*, 8927−8936.

(24) Zhang, L. W.; Gao, S.; Zhang, F.; Yang, K.; Ma, Q. J.; Zhu, L. Activatable Hyaluronic Acid Nanoparticle as a Theranostic Agent for Optical/Photoacoustic Image-Guided Photothermal Therapy. *ACS Nano* **2014**, *8*, 12250−12258.

(25) Sun, X. L.; Huang, X. L.; Yan, X. F.; Wang, Y.; Guo, J. X.; Jacobson, O.; Liu, D. B.; Szajek, L. P.; Zhu, W. L.; Niu, G.; Kiesewetter, D. O.; Sun, S. H.; Chen, X. Y. Chelator-Free $^{64}$Cu-Integrated Gold Nanomaterials for Positron Emission Tomography Imaging Guided Photothermal Cancer Therapy. *ACS Nano* **2014**, *8*, 8438−8446.

(26) Yang, T.; Tang, Y. A.; Liu, L.; Lv, X. Y.; Wang, Q. L.; Ke, H. T.; Deng, Y. B.; Yang, H.; Yang, X. L.; Liu, G.; Zhao, Y. L.; Chen, H. B. Size-Dependent $Ag_2S$ Nanodots for Second Near-Infrared Fluorescence/Photoacoustics Imaging and Simultaneous Photothermal Therapy. *ACS Nano* **2017**, *11*, 1848−1857.

(27) Cheng, L.; Liu, J. J.; Gu, X.; Gong, H.; Shi, X. Z.; Liu, T.; Wang, C.; Wang, X. Y.; Liu, G.; Xing, H. Y.; Bu, W. B.; Sun, B. Q.; Liu, Z. PEGylated $WS_2$ Nanosheets as a Multifunctional Theranostic Agent for in Vivo Dual-Modal CT/Photoacoustic Imaging Guided Photothermal Therapy. *Adv. Mater.* **2014**, *26*, 1886−1893.

(28) Chen, M.; Tang, S. H.; Guo, Z. D.; Wang, X. Y.; Mo, S. G.; Huang, X. Q.; Liu, G.; Zheng, N. F. Core-Shell Pd@Au Nanoplates as



DOI: 10.1021/acsanm.7b00255
*ACS Appl. Nano Mater.* 2018, 1, 820−830

Theranostic Agents for in Vivo Photoacoustic Imaging, CT Imaging, and Photothermal Therapy. *Adv. Mater.* **2014**, *26*, 8210−8216.
(29) Poulose, A. C.; Veeranarayanan, S.; Mohamed, M. S.; Nagaoka, Y.; Aburto, R. R.; Mitcham, T.; Ajayan, P. M.; Bouchard, R. R.; Sakamoto, Y.; Yoshida, Y.; Maekawa, T.; Kumar, D. S. Multi-Stimuli Responsive $Cu_2S$ Nanocrystals as Trimodal Imaging and Synergistic Chemo-Photothermal Therapy Agents. *Nanoscale* **2015**, *7*, 8378−8388.
(30) Tian, G.; Zhang, X.; Zheng, X. P.; Yin, W. Y.; Ruan, L. F.; Liu, X. D.; Zhou, L. J.; Yan, L.; Li, S. J.; Gu, Z. J.; Zhao, Y. L. Multifunctional $Rb_xWO_3$ Nanorods for Simultaneous Combined Chemo-photothermal Therapy and Photoacoustic/CT Imaging. *Small* **2014**, *10*, 4160−4170.
(31) Feng, W.; Zhou, X. J.; Nie, W.; Chen, L.; Qiu, K. X.; Zhang, Y. Z.; He, C. L. Au/Polypyrrole@$Fe_3O_4$ Nanocomposites for MR/CT Dual-Modal Imaging Guided-Photothermal Therapy: An in Vitro Study. *ACS Appl. Mater. Interfaces* **2015**, *7*, 4354−4367.
(32) Wang, Y. H.; Wang, H. G.; Liu, D. P.; Song, S. Y.; Wang, X.; Zhang, H. J. Graphene Oxide Covalently Grafted Upconversion Nanoparticles for Combined NIR Mediated Imaging and Photothermal/Photodynamic Cancer Therapy. *Biomaterials* **2013**, *34*, 7715−7724.
(33) Chen, R.; Wang, X.; Yao, X. K.; Zheng, X. C.; Wang, J.; Jiang, X. Q. Near-IR-Triggered Photothermal/Photodynamic Dual-Modality Therapy System via Chitosan Hybrid Nanospheres. *Biomaterials* **2013**, *34*, 8314−8322.
(34) Vijayaraghavan, P.; Liu, C. H.; Vankayala, R.; Chiang, C. S.; Hwang, K. C. Designing Multi-Branched Gold Nanoechinus for NIR Light Activated Dual Modal Photodynamic and Photothermal Therapy in the Second Biological Window. *Adv. Mater.* **2014**, *26*, 6689−6695.
(35) Guo, W.; Guo, C. S.; Zheng, N. N.; Sun, T. D.; Liu, S. Q. CsxWO$_3$ Nanorods Coated with Polyelectrolyte Multilayers as a Multifunctional Nanomaterial for Bimodal ImagingGuided Photothermal/Photodynamic Cancer Treatment. *Adv. Mater.* **2017**, *29*, 1604157.
(36) Hainfeld, J. F.; Slatkin, D. N.; Focella, T. M.; Smilowitz, H. M. Gold Nanoparticles: A New X-Ray Contrast Agent. *Br. J. Radiol.* **2006**, *79*, 248−253.
(37) Lei, P. P.; Zhang, P.; Yao, S.; Song, S. Y.; Dong, L. L.; Xu, X.; Liu, X. L.; Du, K. M.; Feng, J.; Zhang, H. J. Optimization of $Bi^{3+}$ in Upconversion Nanoparticles Induced Simultaneous Enhancement of Near-Infrared Optical and X-ray Computed Tomography Imaging Capability. *ACS Appl. Mater. Interfaces* **2016**, *8*, 27490−27497.
(38) Zhang, X. D.; Chen, J.; Min, Y.; Park, G. B.; Shen, X.; Song, S. S.; Sun, Y. M.; Wang, H.; Long, W.; Xie, J. P.; Gao, K.; Zhang, L. F.; Fan, S. J.; Fan, F. Y.; Jeong, U. Metabolizable $Bi_2Se_3$ Nanoplates: Biodistribution, Toxicity, and Uses for Cancer Radiation Therapy and Imaging. *Adv. Funct. Mater.* **2014**, *24*, 1718−1729.
(39) Huang, K. Y.; Ma, H. L.; Liu, J.; Huo, S. D.; Kumar, A.; Wei, T.; Zhang, X.; Jin, S. B.; Gan, Y. L.; Wang, P. C.; He, S. T.; Zhang, X. N.; Liang, X. J. Size-Dependent Localization and Penetration of Ultrasmall Gold Nanoparticles in Cancer Cells, Multicellular Spheroids, and Tumors in Vivo. *ACS Nano* **2012**, *6*, 4483−4493.
(40) Zhou, Z. J.; Hu, K. W.; Ma, R.; Yan, Y.; Ni, B.; Zhang, Y. J.; Wen, L. P.; Zhang, Q.; Cheng, Y. Y. Dendritic Platinum-Copper Alloy Nanoparticles as Theranostic Agents for Multimodal Imaging and Combined Chemophotothermal Therapy. *Adv. Funct. Mater.* **2016**, *26*, 5971−5978.
(41) Chen, W. S.; Zeng, K.; Liu, H.; Ouyang, J.; Wang, L. Q.; Liu, Y.; Wang, H.; Deng, L.; Liu, Y. N. Cell Membrane Camouflaged Hollow Prussian Blue Nanoparticles for Synergistic Photothermal-/Chemotherapy of Cancer. *Adv. Funct. Mater.* **2017**, *27*, 1605795.
(42) Yu, X. J.; Li, A.; Zhao, C. Z.; Yang, K.; Chen, X. Y.; Li, W. W. Ultrasmall Semimetal Nanoparticles of Bismuth for Dual-Modal Computed Tomography/Photoacoustic Imaging and Synergistic Thermoradiotherapy. *ACS Nano* **2017**, *11*, 3990−4001.
(43) Li, Z. L.; Liu, J.; Hu, Y.; Li, Z.; Fan, X. L.; Sun, Y.; Besenbacher, F.; Chen, C. Y.; Yu, M. Biocompatible PEGylated Bismuth Nanocrystals: "All-in-One" Theranostic Agent with Triple-Modal Imaging and Efficient in Vivo Photothermal Ablation of Tumors. *Biomaterials* **2017**, *141*, 284−295.
(44) Lei, P. P.; An, R.; Zhang, P.; Yao, S.; Song, S. Y.; Dong, L. L.; Xu, X.; Du, K. M.; Feng, J.; Zhang, H. J. Ultrafast Synthesis of Ultrasmall Poly(Vinylpyrrolidone)-Protected Bismuth Nanodots as a Multifunctional Theranostic Agent for In Vivo Dual-Modal CT/Photothermal-Imaging-Guided Photothermal Therapy. *Adv. Funct. Mater.* **2017**, *27*, 1702018.
(45) Liu, Y. T.; Pan, J.; Feng, S. S. Nanoparticles of Lipid Monolayer Shell and Biodegradable Polymer Core for Controlled Release of Paclitaxel: Effects of Surfactants on Particles Size, Characteristics and in Vitro Performance. *Int. J. Pharm.* **2010**, *395*, 243−250.
(46) Shan, W.; Cui, Y.; Liu, M.; Wu, L.; Xiang, Y. C.; Guo, Q.; Zhang, Z. R.; Huang, Y. Systematic Evaluation of the Toxicity and Biodistribution of Virus Mimicking Mucus-Penetrating DLPC-NPs as Oral Drug Delivery System. *Int. J. Pharm.* **2017**, *530*, 89−98.
(47) Saari, M.; Vidgren, M. T.; Koskinen, M. O.; Turjanmaa, V. M. H.; Nieminen, M. M. Pulmonary Distribution and Clearance of Two Beclomethasone Liposome Formulations in Healthy Volunteers. *Int. J. Pharm.* **1999**, *181*, 1−9.
(48) Sun, C. X.; Wen, L.; Zeng, J. F.; Wang, Y.; Sun, Q.; Deng, L. J.; Zhao, C. J.; Li, Z. One-Pot Solventless Preparation of PEGylated Black Phosphorus Nanoparticles for Photoacoustic Imaging and Photothermal Therapy of Cancer. *Biomaterials* **2016**, *91*, 81−89.
(49) Tao, W.; Zhu, X. B.; Yu, X. H.; Zeng, X. W.; Xiao, Q. L.; Zhang, X. D.; Ji, X. Y.; Wang, X. S.; Shi, J. J.; Zhang, H.; Mei, L. Black Phosphorus Nanosheets as a Robust Delivery Platform for Cancer Theranostics. *Adv. Mater.* **2017**, *29*, 1603276.
(50) Sun, Z. B.; Xie, H. H.; Tang, S. Y.; Yu, X. F.; Guo, Z. N.; Shao, J. D.; Zhang, H.; Huang, H.; Wang, H. Y.; Chu, P. K. Ultrasmall Black Phosphorus Quantum Dots: Synthesis and Use as Photothermal Agents. *Angew. Chem., Int. Ed.* **2015**, *54*, 11526−11530.
(51) Ma, S. H.; Yong, D. M.; Zhang, Y.; Wang, X. J.; Han, X. J. A Universal Approach for the Reversible Phase Transfer of Hydrophilic Nanoparticles. *Chem. - Eur. J.* **2014**, *20*, 15580−15586.
(52) Bi, H. M.; Fu, D. G.; Wang, L.; Han, X. J. Lipid Nanotube Formation Using Space-Regulated Electric Field Above Interdigitated Electrodes. *ACS Nano* **2014**, *8*, 3961−3969.
(53) He, H.; Ji, S. S.; He, Y.; Zhu, A. J.; Zou, Y. L.; Deng, Y. B.; Ke, H. T.; Yang, H.; Zhao, Y. L.; Guo, Z. Q.; Chen, H. B. Photoconversion-Tunable Fluorophore Vesicles for Wavelength-Dependent Photoinduced Cancer Therapy. *Adv. Mater.* **2017**, *29*, 1606690.
(54) Cheng, Y. X.; Zhang, S. P.; Kang, N.; Huang, J. P.; Lv, X. L.; Wen, K.; Ye, S. F.; Chen, Z. W.; Zhou, X.; Ren, L. Polydopamine-Coated Manganese Carbonate Nanoparticles for Amplified Magnetic Resonance Imaging-Guided Photothermal Therapy. *ACS Appl. Mater. Interfaces* **2017**, *9*, 19296−19306.
(55) Zhang, L. Y.; Chen, Y. Y.; Li, Z. L.; Li, L.; Saint-Cricq, P.; Li, C. X.; Lin, J.; Wang, C. G.; Su, Z. M.; Zink, J. I. Tailored Synthesis of Octopus-Type Janus Nanoparticles for Synergistic Actively-Targeted and Chemo-Photothermal Therapy. *Angew. Chem., Int. Ed.* **2016**, *55*, 2118−2121.
(56) Chou, H. T.; Wang, T. P.; Lee, C. Y.; Tai, N. H.; Chang, H. Y. Photothermal Effects of Multi-Walled Carbon Nanotubes on the Viability of BT-474 Cancer Cells. *Mater. Sci. Eng., C* **2013**, *33*, 989−995.
(57) You, Q.; Sun, Q.; Wang, J. P.; Tan, X. X.; Pang, X. J.; Liu, L.; Yu, M.; Tan, F. P.; Li, N. A Single-Light Triggered and Dual-Imaging Guided Multifunctional Platform for Combined Photothermal and Photodynamic Therapy Based on TD-Controlled and ICG-loaded CuS@m$SiO_2$. *Nanoscale* **2017**, *9*, 3784−3796.
(58) Arami, H.; Khandhar, A.; Liggitt, D.; Krishnan, K. M. In Vivo Delivery, Pharmacokinetics, Biodistribution and Toxicity of Iron Oxide Nanoparticles. *Chem. Soc. Rev.* **2015**, *44*, 8576−8607.
(59) Liu, Z.; Liu, X. J.; Ran, X.; Ju, E. G.; Ren, J. S.; Qu, X. G. Single-Layer Tungsten Oxide as Intelligent Photo-Responsive Nanoagents for Permanent Male Sterilization. *Biomaterials* **2015**, *69*, 56−64.


DOI: 10.1021/acsanm.7b00255
*ACS Appl. Nano Mater.* 2018, 1, 820−830

(60) Arami, H.; Khandhar, A.; Liggitt, D.; Krishnan, K. M. In Vivo Delivery, Pharmaco-kinetics, Biodistribution and Toxicity of Iron Oxide Nanoparticles. *Chem. Soc. Rev.* **2015**, *44*, 8576−8607.



DOI: 10.1021/acsanm.7b00255
*ACS Appl. Nano Mater.* 2018, 1, 820−830